Title
A continuum of mineralization from human renal pyramid to stones on stems.

Authors
Sherer, Benjamin A
Chen, Ling
Kang, Misun
et al.

Publication Date
2018-04-01

DOI
10.1016/j.actbio.2018.01.040

Peer reviewed

Acta Biomaterialia 71 (2018) 72–85

Contents lists available at ScienceDirect

Acta Biomaterialia

journal homepage: www.elsevier.com/locate/actabiomat

Full length article

A continuum of mineralization from human renal pyramid to stones on stems

Benjamin A. Sherer [a], Ling Chen [b], Misun Kang [b], Alex R. Shimotake [b], Scott V. Wiener [a], Tom Chi [a], Marshall L. Stoller [a], Sunita P. Ho [a,b,*,1]

[a] Department of Urology, University of California San Francisco, San Francisco, CA 94143, United States
[b] Division of Biomaterials and Bioengineering, Department of Preventive and Restorative Dental Sciences, University of California San Francisco, San Francisco, CA 94143, United States

ARTICLE INFO

Article history:
Received 24 October 2017
Received in revised form 21 December 2017
Accepted 25 January 2018
Available online 9 February 2018

Keywords:
Renal mineralization
Randall's plaque
Nephrolithiasis
Mineral density
Stone composition

ABSTRACT

The development of new modalities for kidney stone prevention rests upon understanding the progression of mineralization within the renal pyramid. The progression from small foci of mineralized volumes within the renal pyramid to larger interstitial plaques that ultimately lead into clinically detectable calcium-based stones on calcium phosphate stems will be presented through correlative microscopy approach. High resolution X-ray computed tomography (micro-XCT), electron microscopy, and energy dispersive X-ray (EDX) compositional analyses of interstitial plaques, stems, and attached stones were performed. Increase in mineral density progressed with mineralization severity, with the highest mineral densities detected within mature Randall's plaque and stems to which kidney stones were attached. EDX analyses revealed variable elemental composition within interstitial plaque, stems, and stones. Micro-XCT reconstructions of stones with stems enabled visualization of unoccluded tubules within stems, with average tubule diameters corresponding to thin limbs of Henle, blood vessels, and collecting ducts. Correlative microscopy confirmed that the progression of mineralization leading to calcium-based nephrolithiasis occurs through a continuum involving four anatomically and structurally distinct biomineralization regions: 1) proximal intratubular mineralization within the renal pyramid; 2) interstitial Randall's plaque near the tip of the papilla; 3) emerging plaque (stems); and, 4) the body of heterogeneous stones.

Statement of Significance

Nephrolithiasis is a common condition affecting nearly 1 in 11 Americans. The most common type of stone, calcium oxalate is known to form on a calcium phosphate deposit on the renal papilla known as Randall's plaque. Novel imaging techniques have identified distinct regions of biomineralization not just at the tip, but throughout the renal papilla. The classic understanding of Randall's plaque formation is reformulated using correlative imaging techniques. This study establishes a stepwise progression of anatomically-specific biomineralization events including, 1) proximal intratubular mineralization within the renal pyramid; 2) interstitial Randall's plaque near the tip of the papilla; 3) emerging plaque (stems); and, 4) the body of heterogeneous stones, and provides insights into the need for plausible site-specific therapeutic intervention.

1. Introduction

It has become axiomatic in the study of nephrolithiasis that particle retention must occur prior to stone formation [1]. Randall's plaques (RP), first identified in 1937, are interstitial calcium phosphate deposits near the tips of renal papillae found in ~20% of kidneys. RP act as an anchor of outward growth for most calcium-based stones without involving tubular lumens. Many stones exhibit a concavity matching the contour of the papillary

Abbreviations: CaOx, Calcium Oxalate; CaP, Calcium Phosphate; CNP, Calcifying Nanoparticle; EDX, Energy-Dispersive X-ray; EM, Electron Microscopy; micro-XCT, High resolution X-ray micro computed tomography; RP, Randall's Plaque; SEM, Scanning Electron Microscopy.

* Corresponding author mailing address at: 707 Parnassus Avenue, D 3212, School of Dentistry, University of California, San Francisco, San Francisco, CA 94143, United States.
Corresponding author's e-mail address: sunita.ho@ucsf.edu (S.P. Ho).
[1] Corresponding author's lab address at: Health Sciences West (HSW) 813, 513 Parnassus Avenue, University of California, San Francisco, San Francisco, CA 94143, United States.

https://doi.org/10.1016/j.actbio.2018.01.040
1742-7061/

surface [2]. Along the concave portion of isolated stones, a dense protuberance of calcium phosphate (herein referred to as the stone's "stem") was often found that was similar in appearance and composition to that found in the interstitial plaque [3,4]. Over the ensuing decades, others have subsequently detected calcium phosphate footprints of RP along concavities of calcium-based stones on stems, believed to have formed in response to emerging RP coming into contact with the uriniferous space [4–6]. Endoscopic observations confirm the frequent presence of mineral deposits along the surface of renal papillae, especially in calcium-based stone formers [7].

Ever since the discovery of RP, innumerable studies have focused on interstitial plaque, protruding plaque (stems), and solitary stones without necessarily correlating them. Therefore, a focused, systematic evaluation of mineralization processes occurring before, during, and after the formation of RP is needed. In this study, we aim to further characterize RP, stems, and attached stones to better elucidate the structural and compositional characteristics contributing to biomineralization in the human kidney leading to nephrolithiasis. To do so, we utilize high resolution X-ray computed tomography (micro-XCT), electron microscopy (EM), and energy dispersive X-ray (EDX) compositional analyses of interstitial plaque, protruding stems, and attached stones. We hypothesize that the typical progression of mineralization resulting in calcium-based nephrolithiasis occurs through a continuum involving four anatomically and structurally distinct biomineralization events: 1) proximal intratubular mineralization within the renal pyramid; 2) interstitial RP near the tip of the papilla; 3) emerging RP forming stems bridging RP to stones; and 4) the body of heterogeneous stones.

2. Materials and Methods

2.1. Specimen collection and mineral density analysis

Institutional review board approval (#14-4533) was obtained to collect and analyze renal pyramids from consenting patients undergoing nephrectomy and stones from patients undergoing percutaneous nephrolithotomy or ureteroscopy, or if found incidentally during nephrectomy. Five representative renal pyramids were selected for analysis by gross appearance such that increasing amounts of Randall's plaque were exemplified. Four stone specimens, amongst over 500 in our catalogue, were judged to have a stem based upon the gross appearance of a narrowed spiculated area, differing in color opposite the smooth surface of the oxalate portion of the stone, or because they were identified during surgery as stones attached through stem to the renal papilla. Specimens were sterilized using 0.31 Mrad of gamma radiation [8]. All specimens were scanned under wet conditions at 4X and 10X magnifications using a micro-XCT scanner (MicroXCT-200, Carl Zeiss Microscopy, Pleasanton, CA) with a #2 source filter, at 40 kVp, and a beam hardening constant of 2. Mineral densities were determined following a detailed calibration protocol of the micro-XCT [9]. An average distribution of lower and higher mineral densities over five specimens also was obtained and compared to lower and higher mineral densities segmented by fitting a Gaussian curve to the average mineral density profile for all five specimens.

2.2. Identification and measurement of patent tubules within stem-stones

After CT scan of the stones, three-dimensional (3D) reconstruction was performed and tubules were visualized by taking an inverse of the reconstructed image (negative Hounsfield units (consistent with empty space)). Customized MATLAB (R2013b, MathWorks Inc., Natick, MA, see appendix) codes were used to analyze diameter of tubules; the path of each tubule could be traced along its length without interruption. A histogram of the tubule diameters showed several peaks and Gaussian functions were generated to best fit the distribution with the peak as a representative value tubule diameter. Significant differences in peak values were considered if the absolute difference between peak values was at least the sum of two half-widths at the half-maximum of the peaks, which in essence is same as full width at half maximum should it be only one peak [10].

2.3. Field emission scanning electron microscopy and compositional analyses of stems and stones

After micro-XCT, all stone specimens were embedded in LR-white resin (Electron Microscopy Sciences, Hatfield, PA), cut along the midline with a slow-speed saw (Isomet, Buehler, Lake Bluff, IL), and polished using basic metallography polishing techniques (series of silicon carbide grit paper with sizes 240, 320, 400, 600, 800, 1200 (Carbimet Paper Strips, Buehler Ltd, Lake Bluff, IL, USA; diamond suspension slurry of grades 6, 3, 1, 0.25 μm (Metadi, Diamond Suspension, H_2O base, Buehler Ltd., Lake Bluff, IL, USA) on polishing cloth (Texmet 1000, Buehler Ltd., Lake Bluff, IL, USA)) [11]. Light (BX51, Olympus Scientific Solutions Americas Corp. Waltham, MA) and field emission scanning electron microscopy (SEM) (SIGMA VP500, Carl Zeiss Microscopy, Pleasanton, CA) techniques were performed on, uncoated, polished surfaces at various magnifications for structural evaluations at multiple length scales at an energy of 0.8 keV. Corresponding elemental information was mapped with an EDX detector at an energy of 10 keV (Bruker AXS, Madison, WI). The detector was calibrated for gain and offset. The error for elemental concentration analysis results were "1–3%", "2–15%" and "∼100%" for concentration ranges ">10%", "1–10%," and "<1%" respectively.

2.4. Statistics

Variation in mineral density was assessed through two different approaches: segmentation with the post-processing AVIZO software (9.0.1, FEI, Hillsboro, Oregon) using water-shed algorithm and via a histogram based on intensity differences within each stone. Peak value estimation was obtained through a Gaussian fit [12,13]. The water-shed method utilizes an iterative computational process to segment regions of distinct composition based upon Hounsfield units (HU). In short, a 'seed' region is manually selected, and the algorithm segments the specimen through comparison of HU between adjacent voxels. When sufficient difference in HU are identified (based upon user specifications and comparison to the mean HU value of the region) the computer will delineate boundaries within the specimen. Gaussian fits were used to identify tubular structures as described in methods Section 2.2.

3. Results

3.1. Multiscale mapping to reveal contextual information of structure, elemental composition of interstitial renal tissues, stems of stones, and stones

Within the renal pyramid of calcium-based stone formers, emerging RP with stems and attached stones are often observed at the tip of papilla (Fig. 1A, panels a and b). Stones develop as an extension of plaque that emerges through the mucosa of the papilla and is exposed to the urinary space within a renal calyx. Higher up in the renal pyramid, intratubular mineral aggregates were present while denser interstitial mineralization (RP) was observed distally

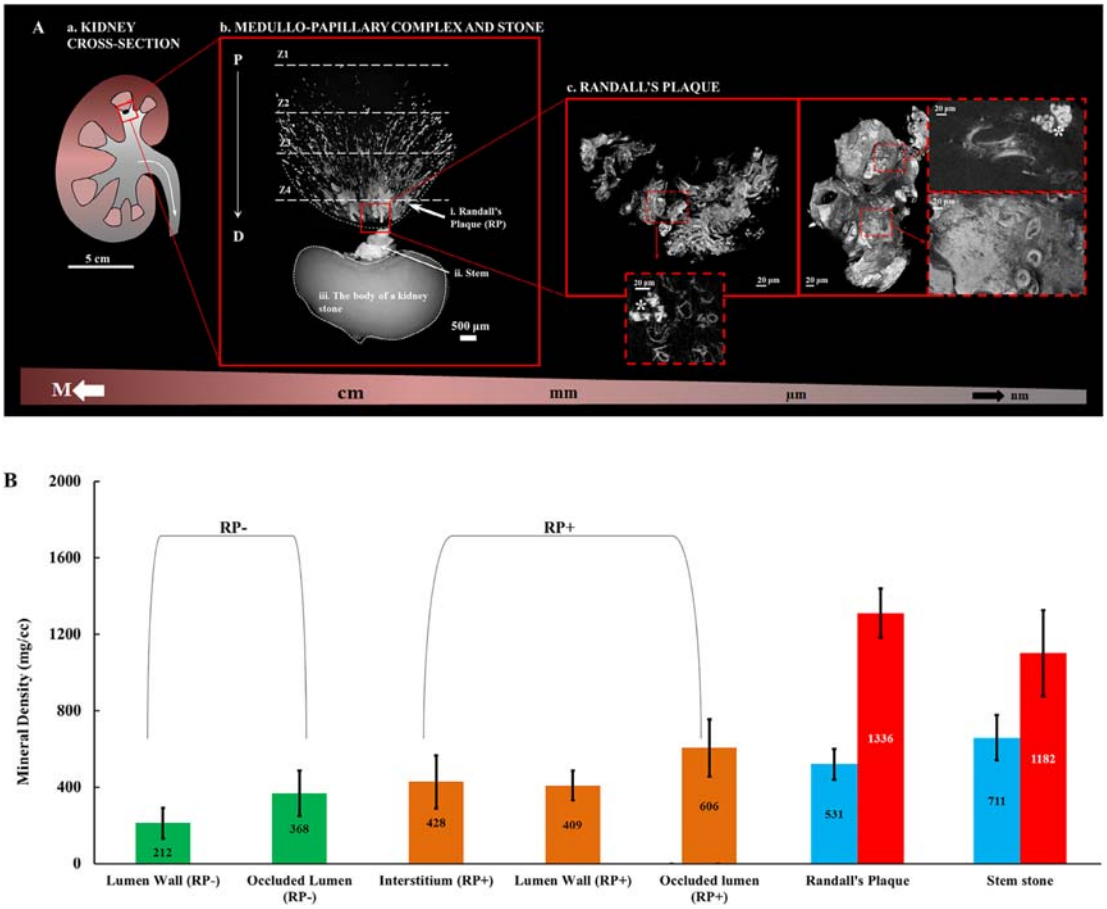

Fig. 1. 1A. A multiscale depiction to provide contextual information for tissue, stem, and stone regions characterized in this study. Intact human renal pyramids (**a**) were analyzed to identify mineralized regions within zones 1 through 4 (Z1–Z4). Panel **b** correlates renal pyramid with Randall's plaque (i) in the distal (D) part of the pyramid with an associated stem (ii) and stone (iii). Under higher magnification (**c**), Randall's plaque at the distal part of the pyramid contains mineralized interstitium and lumen walls, with plaque emerging into collecting ducts (asterisks). Note: Panel b is a virtual overlay of an intact stem with stone extending from a renal pyramid. This image was created to provide contextual information of the stem and stone as a downstream progression of interstitial/Randall's plaque. **1B. Comparison of mineral density values of specific regions within distal interstitial mineralized matrix, Randall's plaque, stem and stone**. Mineralization in RP– specimens (green) was mainly seen in zones 1 and 2 of the renal pyramid. In RP+ specimens (orange), mineralization progressed to more distal location within zones 3 and 4. In specimens with advanced RP and stems, mineralized volumes of both lower (blue) and higher (red) mineral densities were observed. (For interpretation of the references to color in this figure legend, the reader is referred to the web version of this article.)

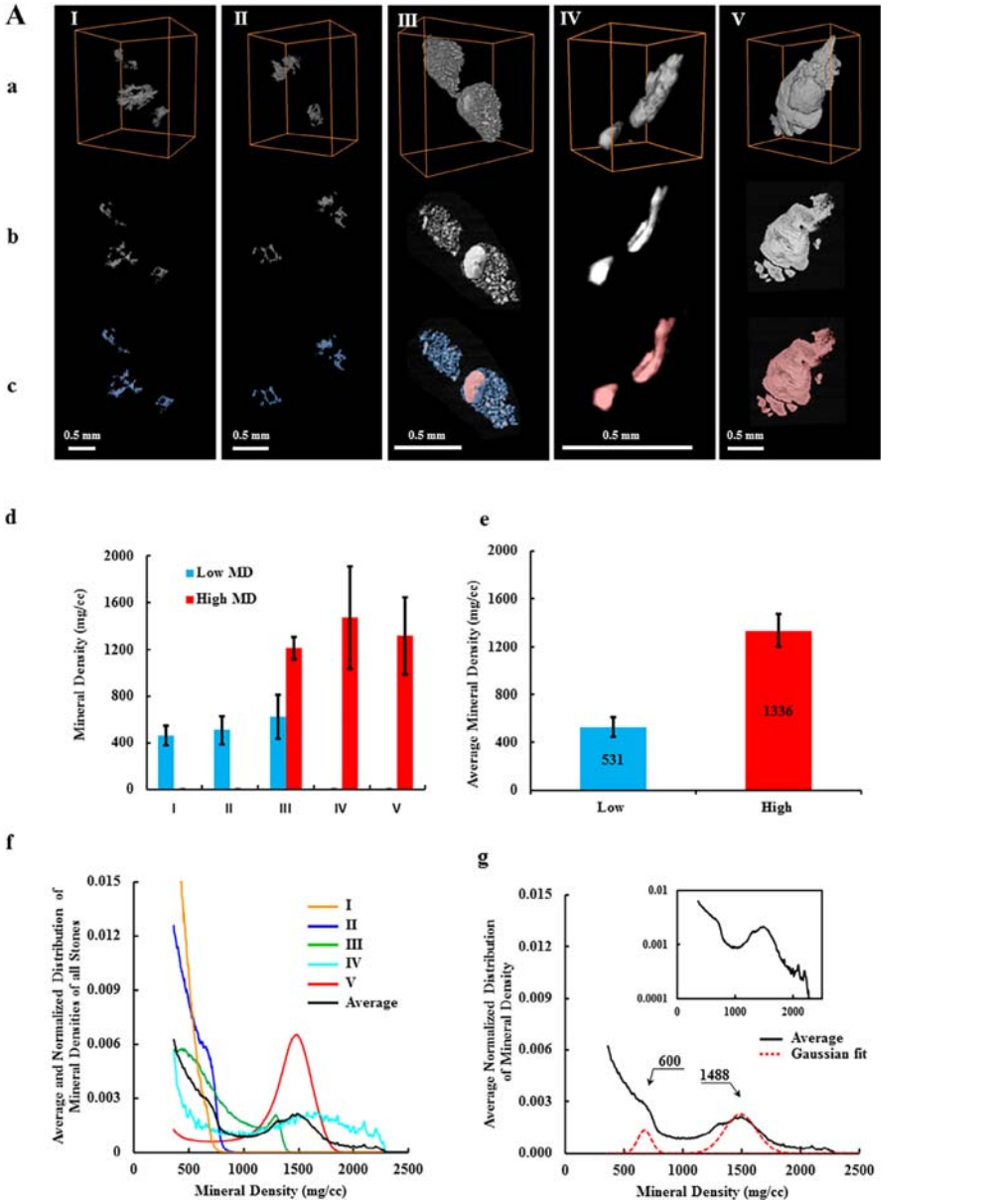

Fig. 2. 2A. Mineral density analyses of Randall's plaque in the renal pyramid at the tissue level. Volumes (row **a**) and virtual sections (row **b**) of biominerals identified in the distal part (Zone 4 in Fig. 1) of various renal pyramids illustrate lower and higher X-ray absorption intensities. Digitally segmented volumes due to different absorption intensities are shown in row **c**. **d.** Histograms illustrate distribution of mineral density (mg/cc) within each specimen (I-V) in addition to background, and average distribution. **e.** Bar plot illustrates average values for lower (blue) and higher (red) MD regions in Randall's plaque delineated by watershed algorithm. **f.** Average and normalized distribution of mineral density in each specimen. **g.** A Gaussian fit illustrates average lower and higher mineral densities within Randall's plaque. A logarithmic plot of normalized mineral distribution is shown as an inset. **2B. Energy dispersive X-ray (EDX) analyses of interstitial mineralized regions of a renal pyramid**. **a.** Representative micrograph of Randall's plaque obtained using a scanning electron microscope (SEM). **b.** Elemental overlay and individual distribution of calcium, phosphorus, and magnesium. **c.** EDX spectra of representative mineralized region of RP (labelled by a red box in a). **d.** Table illustrates elemental content as a percentage of atomic mass. (For interpretation of the references to color in this figure legend, the reader is referred to the web version of this article.)

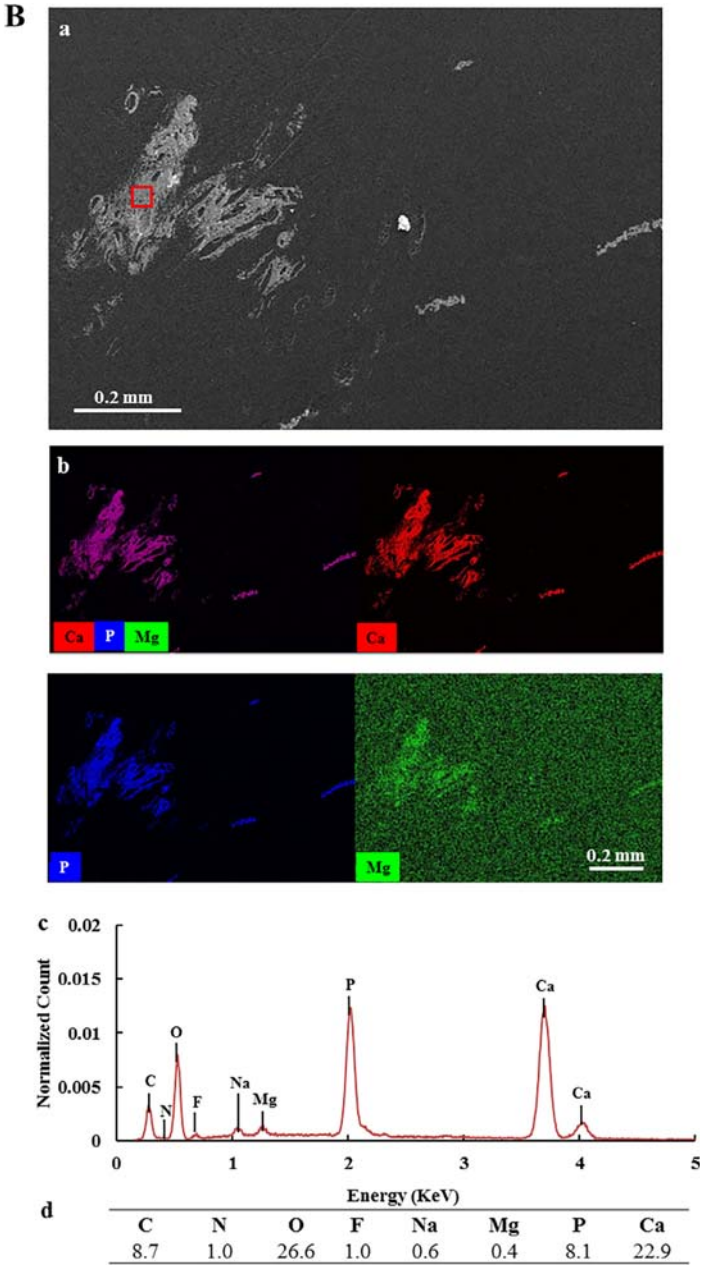

Fig. 2 (*continued*)

(Fig. 1A, panel b). Imaging at a higher magnification with micro-XCT illustrated mineralization within walls of lumens and dense mineralization within the interstitium (Fig. 1A, panel c). The stone and papilla depicted in Fig. 1A were placed together for the purposes of illustrating stones with stems relative to mineralization in the medullo-papillary complex and the renal tip.

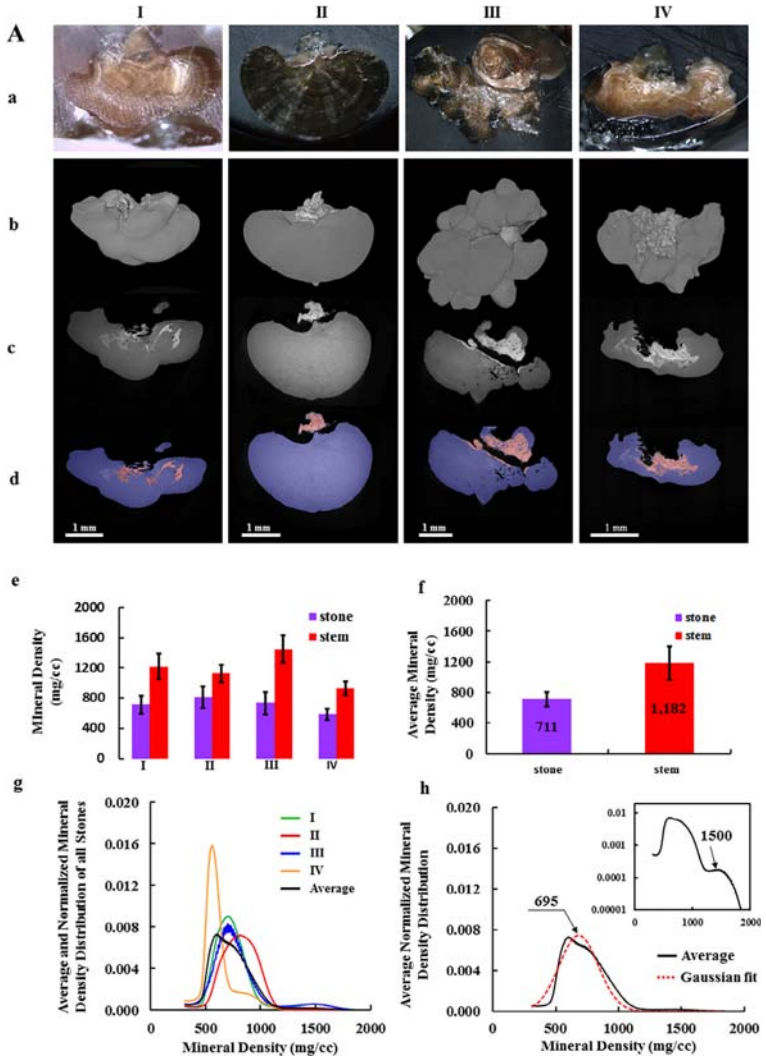

Fig. 3. 3A. Mineral density distributions within stems and stones. a. Various structures and colors in stones were observed using a light microscope at 1X and 1.5X magnifications (row **a**). Digitally reconstructed volumes of stones with intact stems (row **b**) and representative virtual sections (row **c**) illustrated regions of lower and higher X-ray absorption intensities. Digitally segmented regions based on lower and higher X-ray absorption intensities are shown in row **d**. **e.** Histograms of mineral densities (mg/cc) and average distributions within each specimen (I–IV) in addition to background are shown. **f**. Average values for lower and higher MD regions in stems and stones are shown. Significant differences between lower mineral densities within stones (blue) and higher mineral densities within stems (red) are delineated based on water-shed algorithm. **g.** Average and normalized distribution of mineral density in each stem-stone, and (**h**) a Gaussian fit was used to extract on average the lower and higher mineral densities within stem-stones. Logarithmic plots of normalized distribution shown in the inset illustrates a smaller but significant peak in mineral density. **3B. Elemental distributions within stones with stems. a.** Representative virtual micro-CT sections from each stone with intact stems illustrate lower and higher X-ray attenuating regions. **b.** SEM of stem stone interfaces (delineated by white boxes in row **a**). **c.** Correlative elemental map (Ca: calcium; P: phosphorus; Mg: magnesium; Na: sodium; C: carbon; O: oxygen; N: nitrogen; F: Fluorine) of the same region on the sectioned surface shown in row **b**. Rows following row C are individual distributions of elements localized in the same regions. **3C. Energy dispersive X-ray (EDX) analyses of stones with stems.** Column **a** depicts the same regions of interest (stem-stone interfaces) evaluated in 3B. EDX was performed on the numbered regions within the stem-stone interface delineated in Column **a**. Corresponding EDX data is depicted in column **b**. Ca: calcium, P: phosphorus, Mg: magnesium, Na: sodium, C: carbon, O: oxygen, N: nitrogen, F: fluorine; Elemental contents as percent atomic mass are displayed in tables. (For interpretation of the references to color in this figure legend, the reader is referred to the web version of this article.)

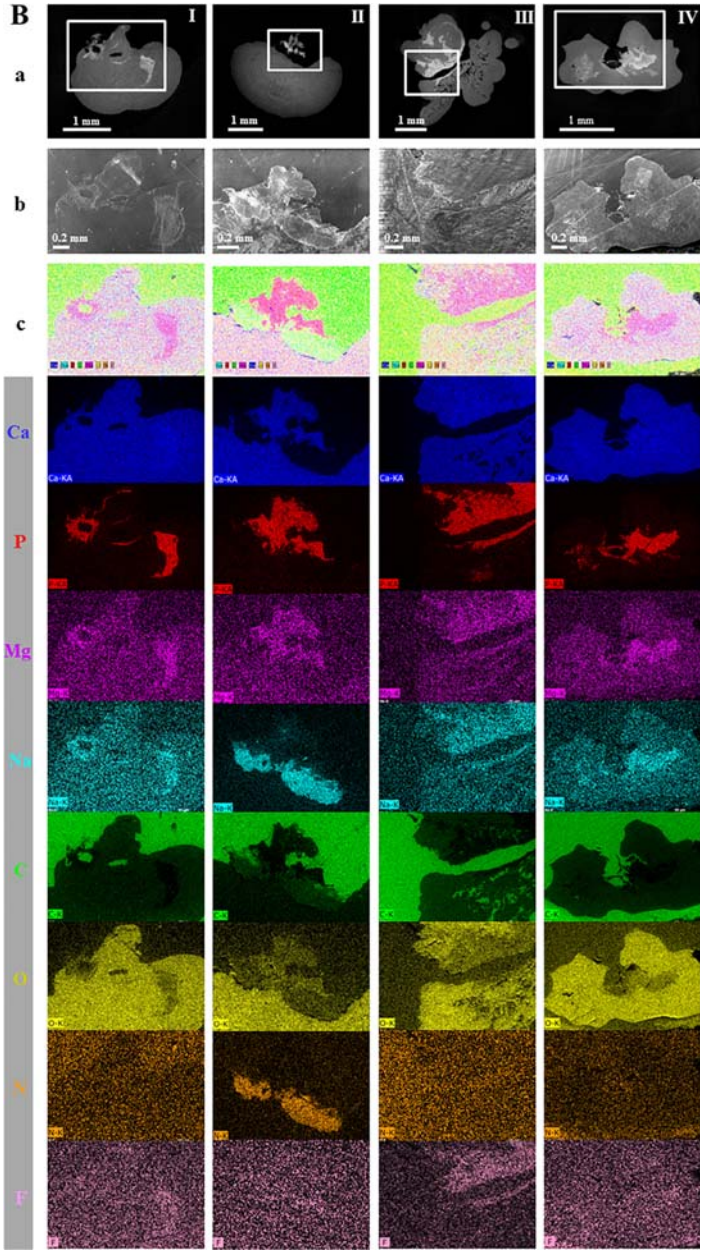

Fig. 3 (*continued*)

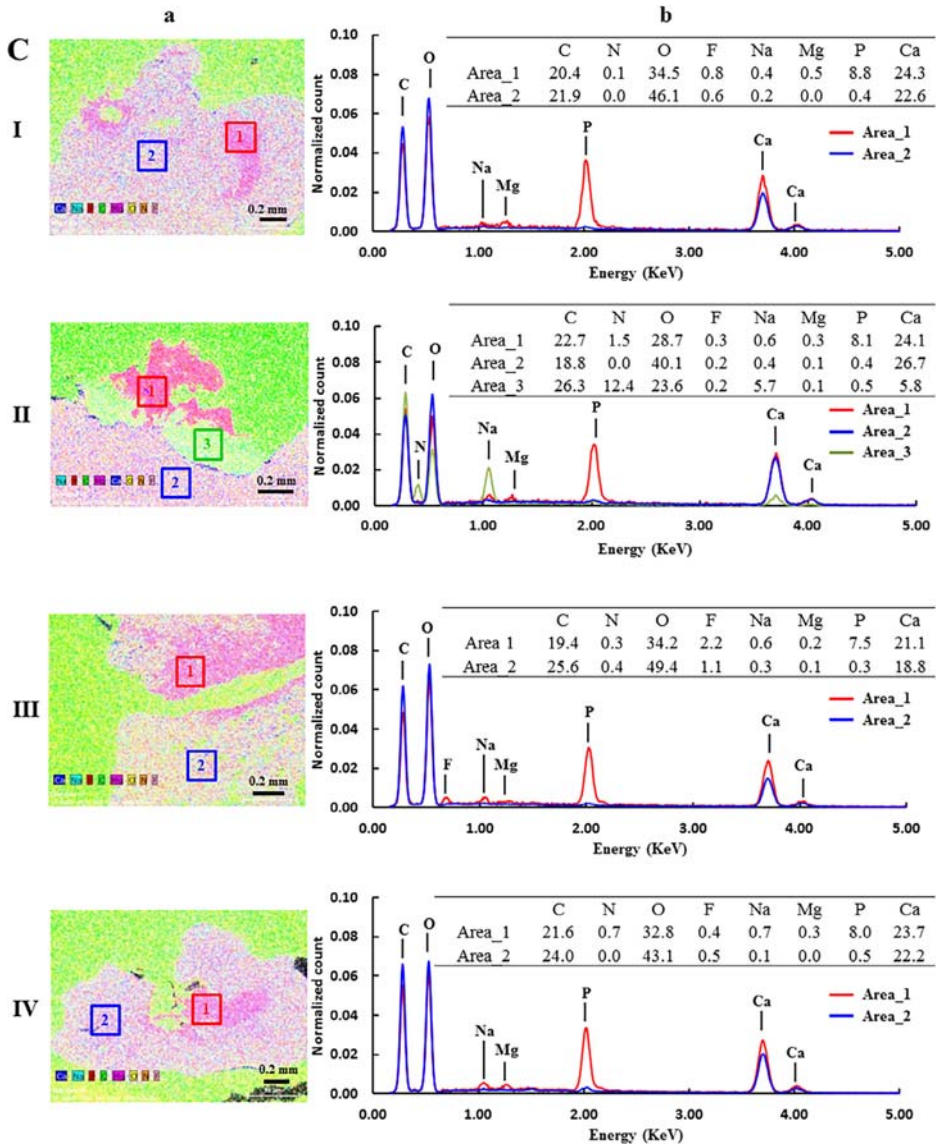

Fig. 3 (*continued*)

3.2. Mineral density and elemental distribution

3.2.1. Randall's plaque

Average mineral density in milligram per centimeter cube (mg/cm^3) in the proximal aspect (Zones 1 and 2) of a "healthy" renal pyramid with scattered intratubular minerals but without distal RP (RP−) was compared to tissue within the same level of a "diseased" renal pyramid containing RP (RP+). Specimens with distal RP had higher mineral densities in the proximal regions (Zones 1 and 2) of the renal pyramid. The progressive spectrum of mineral densities from a normal renal pyramid (RP−) to those containing early RP (RP+, orange) and advanced RP and subsequent stones is shown in Fig. 1B. Average mineral density of the specimens continued to increase from proximal (higher up in the renal pyramid) to distal (within RP, stem, and stone). Micro-XCT of five separate RP (Fig. 2A, rows a–c) revealed anatomically distinct volumes with significantly different mineral densities (Fig. 2A, rows b and c; Fig. 2A-d, 2A-e). A lower mineral density

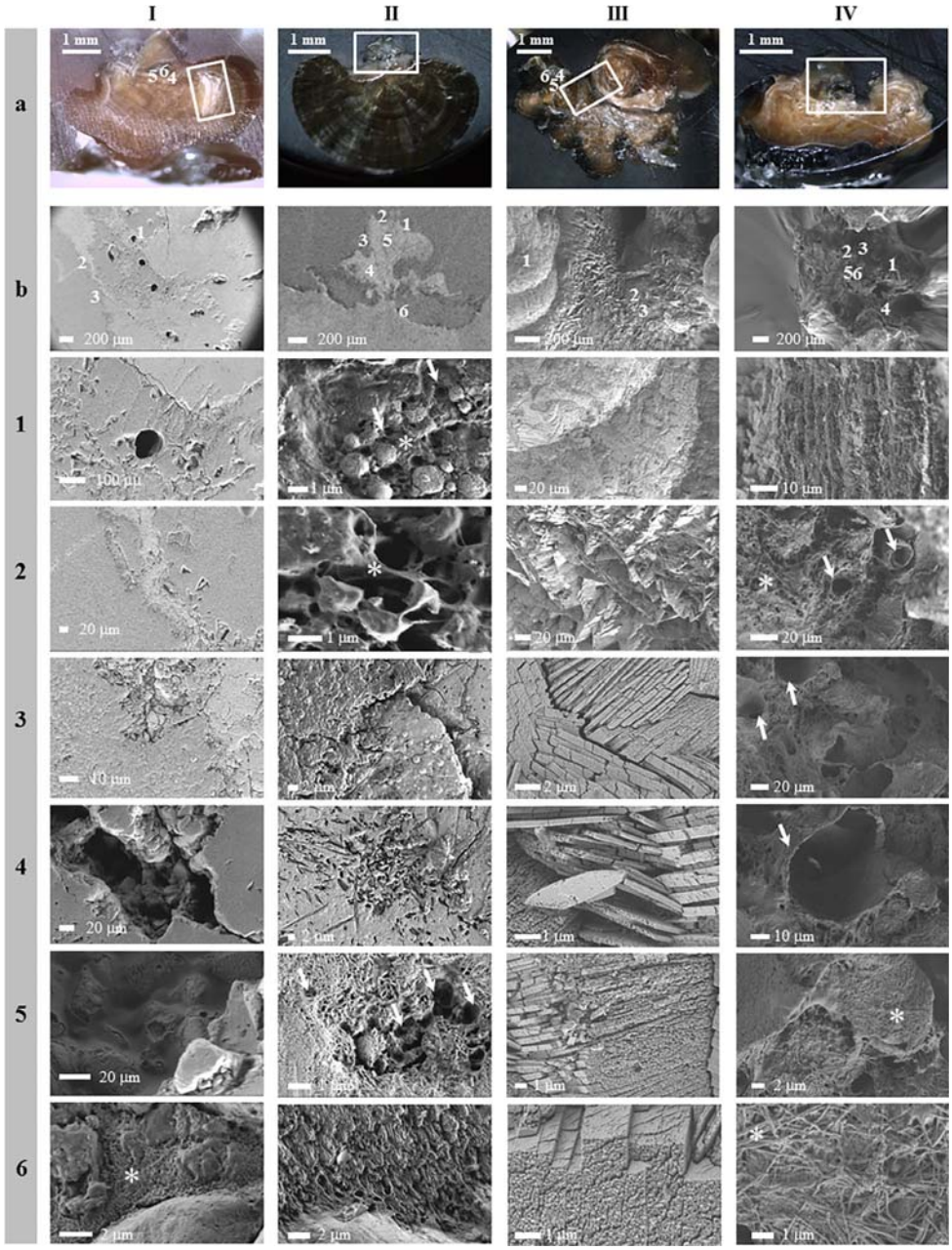

Fig. 4. Light and scanning electron micrographs of stones with stems. a. Light micrographs of cross sections of stones with intact stems taken at 1X-1.5X magnifications illustrate various structural features, layers, and color variation within stems and stones. **b.** SEM micrographs of the regions of interest (white rectangles in row **a**). The areas labeled with numbers in row b are shown at higher magnifications in subsequent rows 1 through 6. Rows 1-6: SEM figures of specific regions of stones with stems at a higher resolution. Figures chosen from locations out of the field of view are not labeled in b. Note: Fibrillar collagen within the stem-stone interface (asterisk); tubule-like casts within stems (arrows).

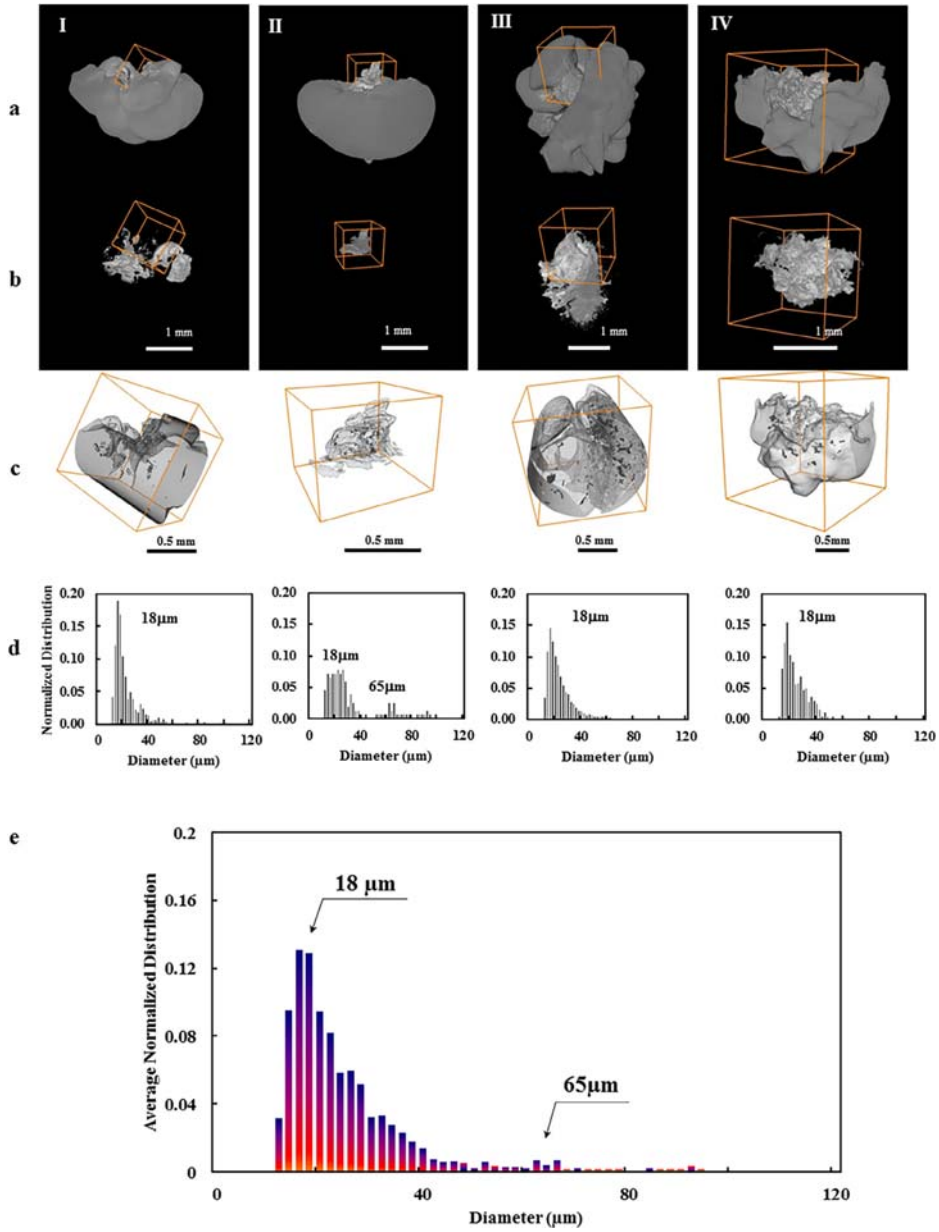

Fig. 5. Stems, stones, and diameter of tubules within stems of stones. a. Digitally reconstructed stems on fully developed stones. **b.** Digitally segmented volumes between stems and stones are shown within cubes respectively. **c.** Higher resolution CT-volumes of stems and stones illustrated tubules within stems (for specimen I) and stones (for specimens II–IV). **d.** Normalized distribution of tubule diameters identified in respective specimens. **e.** Overall tubule diameters from all specimens illustrated a range from 18 through 65 μm

with an average value at 531 mg/cc was observed in early plaque formation (Specimens I-II) and higher mineral density aggregates with an average value of 1330 mg/cc were seen in plaque as the volume fraction of mineral increased (Specimens III–V) (Fig. 2A, row c, and Fig. 2A-d and 2A-e). An average of normalized distributions of mineral density for all five specimens (Fig. 2A-f) confirmed by a Gaussian fit, illustrated two distinct peaks at 600 and 1488 mg/cc (Fig. 2A-g). This was consistent (within error) with the segmentation result obtained using water-shed algorithm (Fig. 2A-e). Mineralized interstitium and lumen walls within RP were observed at higher magnification micro-XCT scans and electron microscopy micrographs (Fig. 1A, panel c; Fig. 2B-a). EDX analyses on RP and intratubular concretions within the tubules illustrated the presence of calcium (Ca), phosphorus (P), and magnesium (Mg) (Fig. 2B-b) supporting that the identified structure was indeed mineralized and were of calcium phosphate composition. Oxygen (O), sodium (Na), nitrogen (N) and carbon (C) were also detected, indicating the presence of organic matter within RP (Fig. 2B-d).

3.2.2. Stone and stems

Micro-XCT of stones with stems illustrated variable mineral density volumes, with higher mineral densities (white on reconstructed volumes and virtual sections) seen within stems and along the stem-stone interface (Fig. 3A, rows a–d). For all specimens, the average mineral density calculated through intensity based (water-shed algorithm) segmentation of the stems (1182 mg/cc) was statistically higher compared to average mineral density (710 mg/cc) of the stones (Fig. 3A-e, 3A-f). The normalized distribution of the mineral density values within each stone is shown in Fig. 3A-g. As a control, Gaussian curve fit to the average normalized distribution of mineral density illustrated two peaks; the peaks were at 695 mg/cc and 1500 mg/cc (Fig. 3A-h), consistent (within error) with the mineral density values obtained using water-shed algorithm (Fig. 3A-f).

In addition, EDX analyses (Fig. 3B, 3C) performed on regions containing stem-stone interfaces illustrated the elemental distribution within stems as they transitioned into the body of stones. Calcium and fluorine were observed in both stem and stone, while phosphorus was mainly located within stems (which correlated to regions of higher mineral density). Sodium and nitrogen were also observed at the interface between stem and stone. Trace amounts of magnesium were detected within stems, while oxygen was mainly concentrated within stones.

3.3. Structural features of stem and stones, and tubule dimensions within stems

Light microscopy of stones with stems (Fig. 4, row a) revealed heterogeneity in stone appearance, color, and laminar growth patterns. All stems were visibly intact on their respective stones. SEM micrographs of regions along the stem-stone interface illustrated evidence of granular architecture and spherical bodies of calcium phosphate (Fig. 4, row b). At a higher magnification, the presence of patent lumens and collagen fibrils within stems were observed. Moving from stem toward the body of stones, a shift from granular to more organized plate-like mineralization was observed (Fig. 4, rows 1–6). Additional features of each stem-stone complex are shown in Supplemental Fig. S1–4. Micro-XCT reconstructions (Fig. 5, rows a–c) of stones with stems illustrated hollow columnar structures indicative of patent tubules, with an average tubule diameter of approximately 18 μm (consistent with vessels and/or thin limbs and loops of Henle) (Fig. 5, rows d and e) and an additional peak at around 65 μm (consistent with collecting ducts).

4. Discussion

4.1. Importance of interstitial plaque in stone formation

Calcium-based stones predominant in calcium oxalate composition, account for approximately 70% of all kidney stones diagnosed in the United States [14]. It is now widely accepted that idiopathic calcium oxalate stones tend to form on stems emerging into the collecting system [15]. Visualization and analyses of the whole papilla in non-stone formers with correlative imaging has identified detectable mineral deposits within the renal pyramid in over 70% of human kidneys [16,17]. Furthermore, patients with higher proportions of RP tend to have low urine volume, high urine calcium, and a heightened subsequent risk of stone events [18,19].

Microscopic medullary and papillary spherical mineral "droplets" in the majority of specimens were identified in hundreds of cadaveric renal units in 1940 s and 1950 s by Anderson and Carr [20,21]. Similarly, calcification within 43 of 62 otherwise normal kidneys, most frequently in the basement membrane of the thin loops of Henle and extending into the surrounding interstitium were identified in 1970 s by Cooke [22]. Laminated spherical bodies of mineral (hereby referred to as calcified nanoparticles [CNP's]) within the interstitium and along basement membranes of tubules within the papilla were observed in 1971 by Haggittusing [23]. An association between small foci of mineralization occurring higher up and rolling toward the medulla to form downstream RP in the papilla was proposed by Bruwer in 1979 [24]. More recently, earliest evidence of mineralization occurring as CNP's near and within the basement membrane of the thin loops of Henle was reported by Evan and colleagues [25]. CNP's are the foci for subsequent interstitial plaque, a finding that is in congruence with many forms of biomineralization prompted by the coalescence of individual calcium phosphate spheres that are 200 nm or less in size [26]. More recently, other groups have identified CNP's at various locations within the interstitium and distally located tubule walls, including vasa recta but not typically near collecting ducts [17,27,28].

4.2. Characterization of mineral in the renal pyramid

Many studies evaluating "early" stone formation within the papilla have been limited to examining endoscopic biopsies of the distal tips of papilla (Fig. 1, Zone 4) [4,6,25]. Micro-XCT and histologic analyses of entire human renal pyramids revealing intratubular mineralization occurring more proximally (Zones 2 and 3) in the papilla, even in specimens without visible RP, suggested that the earliest sites of mineralization are upstream than previously appreciated [16]. Calcium phosphate supersaturation occurs within the thin limbs of the loops of Henle and the collecting ducts, which could allow for calcium phosphate precipitation [29]. Visualization through correlative microscopy provides evidence for the development of nephrolithiasis as interstitial mineralization progresses from small foci of CNPs within the renal pyramid to large interstitial plaque that ultimately leads to clinically detectable emerging RP and subsequently calcium-based stones on calcium phosphate stems.

We postulate that mineralization progresses temporally from medulla toward the tip of the papilla and that there is a shift from intraluminal mineralization in the proximal renal pyramid to extraluminal (within the tubule wall) and interstitial mineralization in the distal papilla (Fig. 1c). The progression of this process is demonstrated on micro-XCT when comparing papilla with increasing amounts of RP (Fig. 2A). Analysis of renal pyramid mineral deposits in RP− and RP+ patients revealed a step-wise, progressive increase in volume and mineral density of concretions

(Fig. 1B, Fig. 2A). In contrast to traditional thinking that RP is uniform in composition and structure, our analyses, revealed heterogeneity in mineral density within individual plaques.

4.3. Composition of interstitial mineral

In recent years, the traditional view of RP as composed of pure calcium phosphate has been challenged with the discovery of whitlockite ($Ca_9(MgFe)(PO_4)_6PO_3OH$) and amorphous calcium phosphate within RP [17,30]. In physiologic systems, there is a pH and concentration driven competition between anions (such as phosphates and oxalates) to calcium as it accumulates in the renal papilla. Within tissues and cells, phosphate binding to calcium tends to stoichiometrically dominate over oxalates, which may explain why RP is predominantly calcium phosphate in composition [31].

The progression of calcium phosphate biomineralization involves various compositional phases, including metastable precursors that subsequently dissolve as precipitation reactions progress. Carbonated apatite, the most predominant component of RP is the least soluble phase of calcium phosphate and tends to form under alkaline conditions. In supersaturated solutions, apatite formation is always associated with a precursor phase [32]. Brushite ($CaHPO_42H_2O$) and octacalcium phosphate ($Ca_8H_2(PO_4)_65H_2O$) are possible precursors to hydroxyl apatite ($Ca_5(PO_4)_3(OH)$) formation, but tend to form in more acidic solutions [32,33]. Amorphous calcium phosphate is the most common precursor of apatite in basic conditions and often consists of spherical calcium phosphate clusters that can aggregate and form larger spheres [34,35]. These structures appear to be analogous to CNP's that have been observed as precursors to RP in the distal papilla. As more CNP's accumulate, they aggregate and fuse to form larger deposits resulting in a plaque within a network of collagen and other proteins [36]. SEM and EDX analyses of plaque and stems (Fig. 3) consistently revealed a central uniform appearance of apatite with lower mineral density, as well as CNPs at the periphery of the expanding plaque. While these structurally and physically distinct entities were observed in various forms of biominerals, the mechanisms by which CNP's aggregate to apatite concretions remain poorly understood [35].

Compositionally, in addition to calcium and phosphate, EDX analysis also revealed detectable presence of oxygen, carbon, sodium, magnesium and fluorine within RP. The presence of fluorine and magnesium in RP and stems may be important for mineralization patterns. The interaction between fluorine, magnesium and calcium is thought to be pH dependent and is a determining factor in the formation of stable calcium phosphate. This may regulate calcium phosphate phase transformation and ultimately the type of calcium phosphate formed [37]. Magnesium is present in a variety of mineralization processes, but does not readily incorporate into the lattice of calcium phosphate salts. However, fluorine reduces the free energy of the apatite. Under conditions of fluctuating pH, reprecipitating apatite can have a higher content of fluorine and could be less soluble than the original apatite [38]. On the other hand, adsorption of magnesium at active surface sites may temporarily block these sites from further mineralization [39]. We propose that RP formation is a coalescence of CNPs, and that magnesium could prevent phase transformation of apatite from amorphous calcium phosphate to a crystalline insoluble phase.

4.4. Characterization of stems and the stone-stem interface

As RP mineralization progresses within the interstitial matrix of the renal pyramid, it emerges through the epithelial lining into the urinary space. It is likely that mature RP (higher mineral density, Fig. 1B) could serve as a stem, sequestering ions from the urine. Striking similarities between RP and stems include higher central mineral density (Fig. 1B), structural patterns, and elemental concentrations of calcium, phosphorus, and magnesium (Fig. 2B, 3B). Furthermore, collagen detected in both stems and RP, confirms their shared interstitial origin. Large fields of type I collagen are frequently observed in proximity to RP and are present in the basement membrane of the thin loops of Henle. These may present an ideal matrix to attract calcium and phosphate specifically in the presence of non collagenous proteins such as osteocalcin [40,41]. Others have identified banding patterns along calcifying strands of plaque in line with interstitial collagen [36].

All stems and stem-stone interfaces evaluated with micro-XCT demonstrated the presence of unoccluded tubules (vessels and thin limbs/loops of Henle), and/or collecting ducts within stems. This may allow unobstructed urinary excretion in the setting of RP and stems despite overlying dense mineralization (Fig. 3). If so, early stones on stems are constantly bathed in supersaturated urine flowing through collecting ducts within interstitial mineral. As mineralization progresses, focal filtration capacity is likely to be reduced leading to higher local concentrations of supersaturated urine. Other experts have postulated that in states of poor hydration and hypercalciuria, calcium and phosphate supersaturation can be routinely expected in the renal pyramid [42]. Furthermore, mineralization in the distal papilla also involves calcium phosphate supersaturation in the setting of high interstitial pH driven by vasa recta [17].

4.5. Structural and compositional shifts from stem to stone

As calcium phosphate stems are exposed to urine within a renal calyx, a shift from an ionically uniform and alkaline interstitial environment to a relatively acidic and variable uriniferous environment may drive mineralization. Although transtubular permeabilities of calcium and phosphates are low in the thin limbs of Henle, they are in close association with vasa recta and collecting ducts that can create a hypertonic and alkaline interstitial environment, allowing calcium phosphate mineralization [41]. Analysis of stems and the stem-stone interface revealed marked heterogeneity in structural and compositional patterns as mineralization transitioned from RP to stems with attached stones. In the formation of calcium oxalate stones, there is an abrupt shift from predominantly calcium phosphate to predominantly calcium oxalate mineralization along the stem-stone interface. Amorphous patterns of minerals, voids, patent lumens, and the presence of collagen were often observed within stems but not within the body of stones. Within stones, mineralization was more uniform and demonstrated classic features of calcium oxalate mineralization including layering and twinning (Fig. 4, Fig. S1–S4). Previous studies have illustrated that early COM layers in stones are interspersed with variable amounts of calcium phosphate, suggesting an interplay between calcium phosphate-supersaturated interstitial fluid and calcium oxalate supersaturated urine [43].

Prior analyses of stems on hundreds of stone specimens revealed that, while stems are predominantly calcium phosphate in ~90% of cases, they may also contain other compositions including whewellite ($CaC_2O_4H_2O$), proteins, glycosaminoglycans, and lipids [44]. The presence of small peptides, proteins, and inorganic ions other than calcium and phosphate can have strong influence on crystallization [33]. In some unique stone formers, stems have even been found to contain significant amounts of sodium hydrogen urate, and uric acid [44]. As expected, EDX analysis revealed calcium to be widely distributed throughout stem and stone (Fig. 3B, 3C) while calcium phosphate was localized to interstitial plaque and stems only, confirming that stems on calcium oxalate stones are a downstream manifestation of RP. Interestingly, magnesium was detected in RP up to the stem-stone interface with minimal magnesium detectable within the body of stones

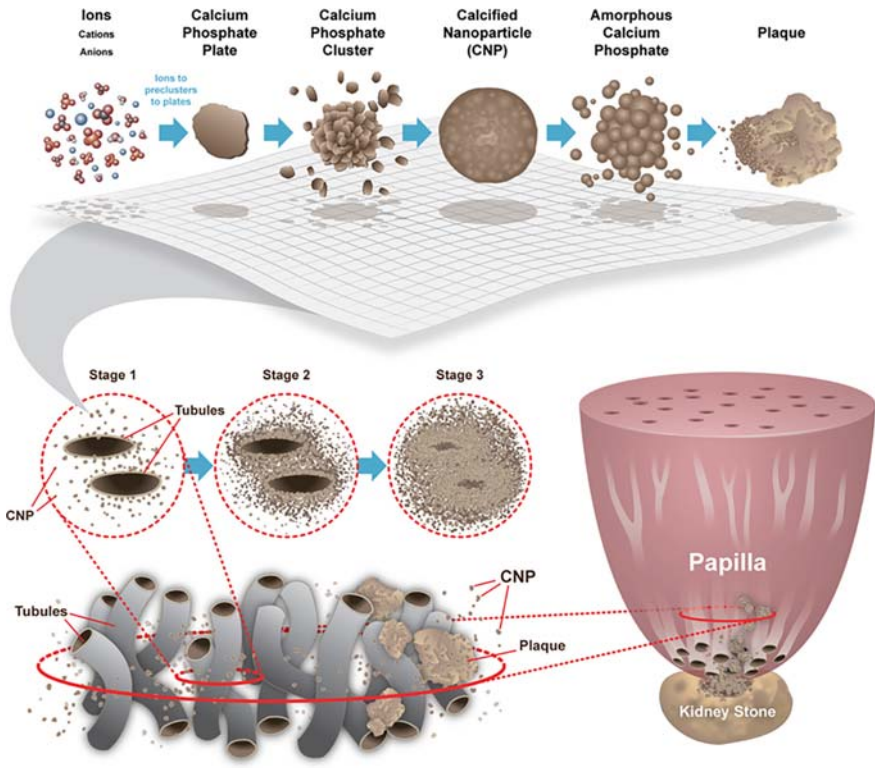

Fig. 6. Proposed progression of biomineralization in the distal papilla: ions to RP toemerging stems and attached stones. Top row: ions coalesce to form preclusters and calcified nanoparticles (CNPs) that subsequently agglomerate into higher ordered calcium phosphate phases (such as amorphous calcium phosphate) which eventually form fully developed RP. Bottom rows: schematic representation of progression of interstitial mineral deposits (stage 1) to agglomerates surrounding tubules (stage 2) to advanced RP (stage 3) that emerges from the papillary tip as stems, forming the foundation for stone growth in the urinary space (bottom right). Note: schematic not drawn to scale.

(Fig. 3B, 3C). Similarly, sodium was routinely detected within stems (especially predominant in stone II, Fig. 3B), but not in the body of stones (Fig. 3b). The role of sodium and magnesium in the progression of stem to the genesis of stones remains unclear, but provide insights into plausible ways to mitigate stems. Not surprisingly, stems were found to have distinct mineral densities and composition similar to RP, but different from their attached stones. Mineral density differences are easily distinguishable on micro-XCT, and can be used to distinguish calcium phosphate (higher mineral density) from calcium oxalate (lower mineral density) by correlating variable mineral density regions with elemental analyses (Fig. 3A, B).

4.6. Limitations

While analyses focused on specimens obtained from idiopathic calcium oxalate stone formers, not all stones form from interstitial plaque. For example, patients with distal tubular acidosis and severe hyperoxaluria (as is seen after intestinal bypass surgery) have been observed to form calcium phosphate stones off of collecting duct "plugs" rather than interstitial plaques [45,46]. Findings from all specimens were consistent, and the power of this study can be increased with more specimens subjected to similar methodologies and analyses.

5. Conclusions

In this study, data acquired from microscopy and spectroscopy techniques are accurate within the resolution limits of the instrumentation. Mineralization within kidneys of common calcium-based stone formers occurs as a continuum starting with proximal mineral deposits that preempt RP formation in the interstitium of the distal renal papilla. Following interaction between anions and cations, early calcium phosphate pre-clusters form CNPs which seem to agglomerate into more complex, higher ordered aggregates resulting in dense interstitial RP near the tip of the papilla (Fig. 6). Additionally, data corroborate with the traditional viewpoint that RP emerges through papillary epithelium and become exposed to the urinary space, allowing a fixed interface (stem) on which calcium-based stones form (Fig. 6). We postulate that partially cell-mediated mineralization processes within the tissue of the papilla convert to a physical chemistry based mineralization process within the urinary space along the stem-stone interface (Fig. 6).

Understanding the earliest sites of mineralization in this continuum is paramount in developing targeted stone prevention therapies. However, as this search is ongoing, we are learning that multiple mechanisms are at play in the heterogeneous environment consisting of various proteins within the renal pyramid. Is RP preventable or reversible? If not, perhaps stone prevention rests

at the stem-stone interface, where targeted therapies could mitigate further mineralization in a uriniferous environment. The uriniferous environment allows calcium oxalate deposition on calcium phosphate nidi emerging from the renal epithelium. The earliest inciting mechanisms in the formation of RP and the transition from calcium phosphate in RP to predominantly calcium oxalate stones continue as a major focus and is an ongoing investigation.

6. Disclosure

The authors report no financial conflicts of interest.

Acknowledgements

Experimental assistance from Ms. Grace Nonomura is greatly appreciated. The authors thank the Biomaterials and Bioengineering Correlative Microscopy Core (http://bbcmc.ucsf.edu), UCSF for the use of MicroXCT-200.

This work was supported by funds from R21 DK109912 (SPH, MLS), and NIDCR/R01DE022032 (SPH).

Appendix A. Supplementary data

Supplementary data associated with this article can be found, in the online version, at https://doi.org/10.1016/j.actbio.2018.01.040.

References

[1] B. Finlayson, F. Reid, The expectation of free and fixed particles in urinary stone disease, Invest. Urol. 15 (1978) 442–448.
[2] A. Randall, The origin and growth of renal calculi, Ann. Surg. 105 (1937) 1009–1027, https://doi.org/10.1097/00000658-193706000-00014.
[3] A. Randall, Papillary pathology as a precursor of primary renal calculus, J. Urol. 44 (1940) 580–589, https://doi.org/10.1016/S0022-5347(17)71305-5.
[4] A.P. Evan, F.L. Coe, J.E. Lingeman, Y. Shao, A.J. Sommer, S.B. Bledsoe, J.C. Anderson, E.M. Worcester, Mechanism of formation of human calcium oxalate renal stones on Randall's plaque, Anat. Rec. (Hoboken) 290 (2007) 1315–1323, https://doi.org/10.1002/ar.20580.
[5] L. Cifuentes Delatte, J. Miñón-Cifuentes, J.A. Medina, New studies on papillary calculi, J. Urol. 137 (1987) 1024–1029.
[6] A.P. Evan, F.L. Coe, S.R. Rittling, S.M. Bledsoe, Y. Shao, J.E. Lingeman, E.M. Worcester, Apatite plaque particles in inner medulla of kidneys of calcium oxalate stone formers: osteopontin localization, Kidney Int. 68 (2005) 145–154, https://doi.org/10.1111/j.1523-1755.2005.00388.x.
[7] R.K. Low, M.L. Stoller, Endoscopic mapping of renal papillae for Randall's plaques in patients with urinary stone disease, J. Urol. 158 (1997) 2062–2064.
[8] D.S. Brauer, K. Saeki, J.F. Hilton, G.W. Marshall, S.J. Marshall, Effect of sterilization by gamma radiation on nano-mechanical properties of teeth, Dent. Mater. 24 (2008) 1137–1140, https://doi.org/10.1016/j.dental.2008.02.016.
[9] S.I. Djomehri, S. Candell, T. Case, A. Browning, G.W. Marshall, W. Yun, S.H. Lau, S. Webb, S.P. Ho, Mineral density volume gradients in normal and diseased human tissues, PLoS One. 10 (2015) e0121611, https://doi.org/10.1371/journal.pone.0121611.
[10] B.A. Sherer, L. Chen, F. Yang, K. Ramaswamy, D.W. Killilea, R.S. Hsi, M.L. Stoller, S.P. Ho, Heterogeneity in calcium nephrolithiasis: a materials perspective, J. Mater. Res. 32 (2017) 2497–2509, https://doi.org/10.1557/jmr.2017.153.
[11] S.P. Ho, H. Goodis, M. Balooch, G. Nonomura, S.J. Marshall, G. Marshall, The effect of sample preparation technique on determination of structure and nanomechanical properties of human cementum hard tissue, Biomaterials. 25 (2004) 4847–4857.
[12] H. Digabel, C. Lantuéjoul, Iterative algorithms, in: Proc. 2nd Eur. Symp. Quant. Anal. Microstruct. Mater. Sci. Biol. Med., Riederer Verlag, Stuttgart, West Germany, 1978, p. 8.
[13] J.B.T.M. Roerdink, A. Meijster, The watershed transform: definitions, algorithms and parallelization strategies, Fundam. Informaticae. 41 (2000) 187–228, https://doi.org/10.3233/FI-2000-411207.
[14] O.W. Moe, Kidney stones: pathophysiology and medical management, Lancet 367 (2006) 333–344, https://doi.org/10.1016/S0140-6736(06)68071-9.
[15] E. Letavernier, S. Vandermeersch, O. Traxer, M. Tligui, L. Baud, P. Ronco, J.-P. Haymann, M. Daudon, Demographics and characterization of 10,282 Randall plaque-related kidney stones: a new epidemic?, Medicine (Baltimore) 94 (2015) e566, https://doiorg/10.1097/MD.0000000000000566.
[16] R.S. Hsi, K. Ramaswamy, S.P. Ho, M.L. Stoller, The origins of urinary stone disease: upstream mineral formations initiate downstream Randall's plaque, BJU Int. 119 (2017) 177–184, https://doi.org/10.1111/bju.13555.
[17] C. Verrier, D. Bazin, L. Huguet, O. Stéphan, A. Gloter, M.-C. Verpont, V. Frochot, J.-P. Haymann, I. Brocheriou, O. Traxer, M. Daudon, E. Letavernier, Topography, composition and structure of incipient Randall plaque at the nanoscale level, J. Urol. 196 (2016) 1566–1574, https://doi.org/10.1016/j.juro.2016.04.086.
[18] R.L. Kuo, J.E. Lingeman, A.P. Evan, R.F. Paterson, J.H. Parks, S.B. Bledsoe, L.C. Munch, F.L. Coe, Urine calcium and volume predict coverage of renal papilla by Randall's plaque, Kidney Int. 64 (2003) 2150–2154, https://doi.org/10.1046/j.1523-1755.2003.00316.x.
[19] S.C. Kim, F.L. Coe, W.W. Tinmouth, R.L. Kuo, R.F. Paterson, J.H. Parks, L.C. Munch, A.P. Evan, J.E. Lingeman, Stone formation is proportional to papillary surface coverage by Randall's plaque discussion 119, J. Urol. 173 (2005) 117–119, https://doi.org/10.1097/01.ju.0000147270.68481.ce.
[20] L. Anderson, J.R. McDONALD, The origin, frequency, and significance of microscopic calculi in the kidney, Surg. Gynecol. Obstet. 82 (1946) 275–282.
[21] R.J. Carr, A new theory on the formation of renal calculi, Br. J. Urol. 26 (1954) 105–117.
[22] S.A. Cooke, The site of calcification in the human renal papilla, Br. J. Surg. 57 (1970) 890–896.
[23] R.C. Haggitt, J.A. Pitcock, Renal medullary calcifications: a light and electron microscopic study, J. Urol. 106 (1971) 342–347.
[24] A. Bruwer, Primary renal calculi: Anderson-Carr-Randall progression?, AJR Am. J. Roentgenol. 132 (1979) 751–758, https://doi.org/10.2214/ajr.132.5.751.
[25] A.P. Evan, J.E. Lingeman, F.L. Coe, J.H. Parks, S.B. Bledsoe, Y. Shao, A.J. Sommer, R.F. Paterson, R.L. Kuo, M. Grynpas, Randall's plaque of patients with nephrolithiasis begins in basement membranes of thin loops of Henle, J. Clin. Invest. 111 (2003) 607–616, https://doi.org/10.1172/JCI17038.
[26] M.H. Beer, R.S. Porter, T. V Jones, eds., Musculoskeletal and Connective Tissue Disorders., in: Merck Man. Diagnosis Ther., 18th ed., Wiley, Whitehouse Station, NJ, 2006: p. 304.
[27] M.L. Stoller, M.V. Meng, H.M. Abrahams, J.P. Kane, The primary stone event: a new hypothesis involving a vascular etiology, J. Urol. 171 (2004) 1920–1924, https://doi.org/10.1097/01.ju.0000120291.90839.49.
[28] N. Ciftçioğlu, K. Vejdani, O. Lee, G. Mathew, K.M. Aho, E.O. Kajander, D.S. McKay, J.A. Jones, M.L. Stoller, Association between Randall's plaque and calcifying nanoparticles, Int. J. Nanomedicine. 3 (2008) 105–115.
[29] J.R. Asplin, N.S. Mandel, F.L. Coe, Evidence of calcium phosphate supersaturation in the loop of Henle, Am. J. Physiol. 270 (1996) F604–F613.
[30] H.-G. Tiselius, B. Lindbäck, A.-M. Fornander, M.-A. Nilsson, Studies on the role of calcium phosphate in the process of calcium oxalate crystal formation, Urol. Res. 37 (2009) 181–192, https://doi.org/10.1007/s00240-009-0191-7.
[31] F.U. Beil, D. von Chak, W. Hasselbach, H.H. Weber, Competition between oxalate and phosphate during active calcium accumulation by sarcoplasmic vesicles, Zeitschrift Fur Naturforschung. Sect. C, Biosci. 32 (1977) 281–287.
[32] B. Finlayson, Physicochemical aspects of urolithiasis, Kidney Int. 13 (1978) 344–360, https://doi.org/10.1038/ki.1978.53.
[33] L. Wang, G.H. Nancollas, Calcium orthophosphates: crystallization and dissolution, Chem. Rev. 108 (2008) 4628–4669, https://doi.org/10.1021/cr0782574.
[34] A.S. Posner, F. Betts, Synthetic amorphous calcium phosphate and its relation to bone mineral structure, Acc. Chem. Res. 8 (1975) 273–281, https://doi.org/10.1021/ar50092a003.
[35] A. Dey, P.H.H. Bomans, F.A. Müller, J. Will, P.M. Frederik, G. de With, N.A.J.M. Sommerdijk, The role of prenucleation clusters in surface-induced calcium phosphate crystallization, Nat Mater. 9 (2010) 1010–1014, https://doi.org/10.1038/nmat2900.
[36] S.R. Khan, D.E. Rodriguez, L.B. Gower, M. Monga, Association of Randall plaque with collagen fibers and membrane vesicles, J. Urol. 187 (2012) 1094–1100, https://doi.org/10.1016/j.juro.2011.10.125.
[37] R.Z. LeGeros, P. Morales, Renal stone crystals grown in gel systems. A preliminary report, Invest. Urol. 11 (1973) 12–20.
[38] A.C. Ramsey, E.J. Duff, L. Paterson, J.L. Stuart, The uptake of F- by hydroxyapatite at varying pH, Caries Res. 7 (1973) 231–244.
[39] E.D. Eanes, S.L. Rattner, The effect of magnesium on apatite formation in seeded supersaturated solutions at pH 7.4, J. Dent. Res. 60 (1981) 1719–1723, https://doi.org/10.1177/00220345810600091401.
[40] L. Chen, R. Hsi, F. Yang, M. Kang, B. Sherer, M.L. Stoller, S.P. Ho, Anatomically-specific intratubular and interstitial biominerals in the human renal medullo-papillary complex, PLoS One (2017). in press.
[41] B.R. Matlaga, F.L. Coe, A.P. Evan, J.E. Lingeman, The role of Randall's plaques in the pathogenesis of calcium stones, J. Urol. 177 (2007) 31–38, https://doi.org/10.1016/j.juro.2006.08.088.
[42] D.A. Bushinsky, Nephrolithiasis: site of the initial solid phase, J. Clin. Invest. 111 (2003) 602–605, https://doi.org/10.1172/JCI18016.
[43] I. Sethmann, G. Wendt-Nordahl, T. Knoll, F. Enzmann, L. Simon, H.-J. Kleebe, Microstructures of Randall's plaques and their interfaces with calcium oxalate monohydrate kidney stones reflect underlying mineral precipitation mechanisms, Urolithiasis 45 (2017) 235–248, https://doi.org/10.1007/s00240-016-0925-2.
[44] M. Daudon, O. Traxer, P. Jungers, D. Bazin, Stone morphology suggestive of Randall's plaque, in: AIP Conf. Proc., AIP, 2007, pp. 26–34, https://doi.org/10.1063/1.2723556.
[45] F.L. Coe, A.P. Evan, E.M. Worcester, J.E. Lingeman, Three pathways for human kidney stone formation, Urol. Res. 38 (2010) 147–160, https://doi.org/10.1007/s00240-010-0271-8.
[46] A.P. Evan, Physiopathology and etiology of stone formation in the kidney and the urinary tract, Pediatr. Nephrol. 25 (2010) 831–841, https://doi.org/10.1007/s00467-009-1116-y.